





Analytical Signal-to-Noise Ratio Model on Frequency-Scanned Brillouin Optical Time-Domain Reflectometry

Simeng Jin , Zhisheng Yang , *Member, IEEE, Member, OSA*, Xiaobin Hong , *Member, OSA*, and Jian Wu , *Member, IEEE, Member, OSA*

Abstract—An analytical signal-to-noise ratio (SNR) model of standard frequency-scanned Brillouin optical time-domain reflectometry (FS-BOTDR) is established, by comprehensively taking into account nearly all non-negligible signal and noise terms with substantial impact on the sensing performance. The accuracy and generality of the proposed model are experimentally validated, supported by the fact that under various experimental conditions all experimental results are in good quantitative agreement with theoretical calculations. Serving as a theoretical tool, the established model makes it possible to accurately anticipate and comprehensively interpret the SNR behavior of the FS-BOTDR under any given measurement condition, without the need to construct an experimental system or carry out experiments. It also enables theoretically quantifying the SNR difference between FS-BOTDR and other distributed optical fiber sensors that already have mature SNR models. Furthermore, the proposed model provides guidelines on optimizing system parameters towards the highest possible SNR with minimized energy consumption.

Index Terms—Brillouin scattering, distributed optical fiber sensors, optical fibers, signal-to-noise ratio.

I. INTRODUCTION

BRILLOUIN optical time-domain reflectometry (BOTDR) is a widely studied distributed optical fiber sensing technique, capable of spatially interrogating environmental quantities throughout the sensing fiber with a large dynamic measurand range [1], [2], [3], [4], [5]. BOTDR that utilizes spontaneous Brillouin scattering (SpBS), featuring single-end fiber access, typically employs a heterodyne detection scheme to magnify the weak SpBS signal, whilst converting the Brillouin information from the optical domain to an electrical-domain beating signal

Manuscript received 16 December 2023; revised 25 March 2024 and 29 April 2024; accepted 6 May 2024. Date of publication 9 May 2024; date of current version 16 August 2024. This work was supported in part by the National Natural Science Foundation of China under Grant 62375023 and Grant 62275028, in part by Xiaomi Young Talents Program, in part by Beijing Nova Program under Grant Z211100002121074, and in part by the Fundamental Research Funds for the Central Universities under Grant 2023RC51. (*Corresponding author: Zhisheng Yang.*)

The authors are with the State Key Laboratory of Information Photonics and Optical Communications, Beijing University of Posts and Telecommunications, Beijing 100876, China (e-mail: jinsimeng@bupt.edu.cn; zhisheng.yang@bupt.edu.cn; xbhong@bupt.edu.cn; jianwu@bupt.edu.cn).

Color versions of one or more figures in this article are available at <https://doi.org/10.1109/JLT.2024.3398634>.

Digital Object Identifier 10.1109/JLT.2024.3398634

through the photodetection process [1], [2], [3], [4], [5], [6], [7], [8], [9], [10], [11], [12]. The local Brillouin spectrum of BOTDR can be reconstructed by either directly acquiring the beating signal with subsequent digital signal processing [6], [7], [8], or acquiring the temporal envelope of the beating signal at each step of a frequency scanning process [9], [10], [11], [12]. The latter approach, here referred to as frequency-scanned BOTDR (FS-BOTDR), presents a much lower hardware and software overhead, and is therefore preferable realizing a long sensing range that corresponds to a large number of data points to be processed.

As both the manipulation and post-processing procedures of FS-BOTDR are in total similarity with those of standard Brillouin optical time-domain analysis (BOTDA) [13], [14], [15], these two techniques share a similar methodology in terms of evaluating the performance of sensing system. This means that any relevant know-how developed for one of these two techniques may directly benefit the other. For instance, the formula able to theoretically estimate the uncertainty of the Brillouin frequency shift (BFS) σ_v in BOTDA, i.e., $\sigma_v = \sqrt{3\delta\Delta v_B/4/SNR}$ [16], may be directly reused for FS-BOTDR by replacing the relevant parameters, namely the signal-to-noise ratio (SNR) of the measurement, the frequency scanning step δ and the full width at half maximum (FWHM) of the local Brillouin spectrum Δv_B . This highlights the significance on the establishment of SNR models for both techniques. For standard BOTDA a mature SNR model has been established [17], which has even been recently extended for advanced BOTDA techniques [18], [19]; however, till now the models dealing with the SNR of FS-BOTDR present in literature remain incomplete. They are originally established to analyze a specific technical detail such as the impact of number of wavelength used [20], [21], [22] or the pulse extinction ratio [23], [24], but have not yet precisely taken into account either the signal-amplified detection noise originating from the envelope detection process, or the polarization fading noise caused by the use of polarization scrambler (PSc). This lack of clarity regarding the overall impact of noises on the measurement of FS-BOTDR imposes mismatch between the theoretically estimated and actual SNRs, hindering the accurate anticipation of the system performance and the optimization of system parameters. Moreover, the absence of a complete SNR model of FS-BOTDR critically prevents

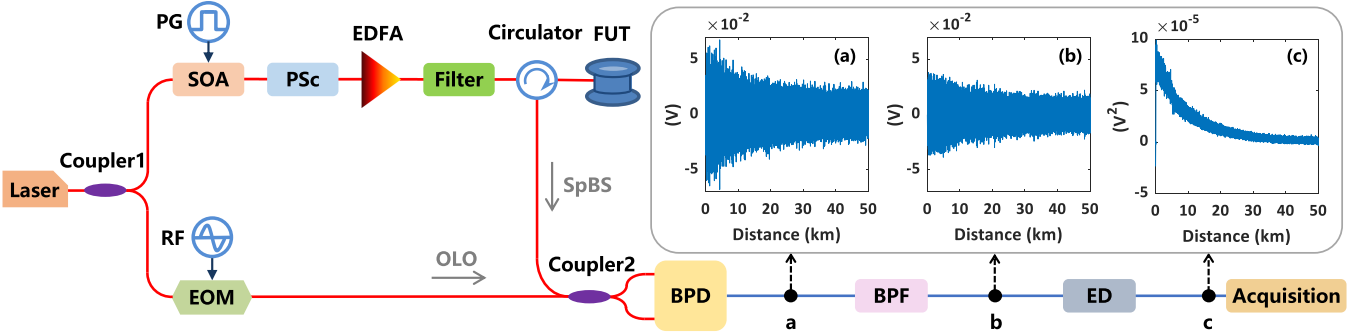


Fig. 1. The standard configuration of FS-BOTDR system and the exemplified distance-domain output of (a) a balanced photodetector (BPD); (b) A bandpass filter (BPF); and (c) An envelope detector (ED). PG: Pulse generator; SOA: Semiconductor optical amplifier; PSc.: Polarization scrambler; EDFA: Erbium-doped fiber amplifier; FUT: Fiber under test; RF: Radio frequency; EOM: Electro-optic modulator.

theoretically quantifying its performance difference with respect to BOTDA, though by common sense the latter utilizing stimulate Brillouin scattering (SBS) in principle corresponds to a higher SNR.

In this paper, a more complete SNR model of the standard FS-BOTDR system, thoroughly taking into account almost all signal and noise terms with substantial impact on the sensing performance, is established for the first time to the best of our knowledge, enabling a comprehensive understanding of FS-BOTDR system on how system parameters affect the overall performance. Results point out that, there are signal-dependent noises arising from the envelope detection process present in FS-BOTDR system, typically including polarization noise and signal-amplified detection noise, which have not been adequately addressed in previous literature whereas actually impact significantly on the SNR behavior. The established SNR model is experimentally validated in both long-range and short-range sensing scenarios with distinct spatial resolutions. Furthermore, by combining with the noise analysis of BOTDA that has existed in the literature [17], [18], [19], the proposed SNR model of FS-BOTDR makes it possible to quantitatively compare the performance difference between these two major techniques in Brillouin distributed sensing area under any measurement condition.

II. STANDARD FS-BOTDR CONFIGURATION AND SNR MODELLING

For the sake of fundamentality, the basic SNR model of standard FS-BOTDR is here step-by-step established by describing its working principle based on the typical configuration shown in Fig. 1. Using this established model as a basis, more dedicated models for other specific FS-BOTDR configurations may be developed accordingly. In Fig. 1, a continuous wave emitted from a narrow linewidth distributed feedback laser is split into two branches by an optical coupler (Coupler1). In the upper branch, the light is intensity-modulated to an optical pulse via a semiconductor optical amplifier (SOA) driven by a pulse generator (PG). Before being launched into the fiber under test (FUT), the optical pulse successively passes through a polarization scrambler (PSc) to mitigate the polarization fading effect, an erbium-doped fiber amplifier (EDFA) to optimize the

pulse peak power, and an optical filter to reduce the broadband optical noise from the EDFA. The distance-dependent power of the SpBS signal, designated as $P_S(z)$, being the summation of the Stokes signal power $P_{S1}(z)$ and Anti-Stokes signal power $P_{S2}(z)$, can be expressed as:

$$P_S(z) = P_{S1}(z) + P_{S2}(z) = \frac{k_S c P_p D_p e^{-2\alpha z}}{N} \quad (1)$$

where k_S is the backscattering coefficient of SpBS in silica, typically in the order of magnitude of $3 \times 10^{-10}/\text{m}$ (-95 dB/m in logarithmic scale) [25]; c is the mode group velocity in vacuum; P_p and D_p are the peak power and duration of the incident pulse, respectively; N is the effective group index of the propagating mode in the fiber; α is the fiber attenuation coefficient. In the lower branch, the laser beam is injected into an electro-optic modulator (EOM) to generate a carrier-suppressed double-sideband wave. This wave acts as the optical local oscillator (OLO), with an optical power of $P_{Lo} = P_{Lo1} + P_{Lo2}$, P_{Lo1} and P_{Lo2} being the optical power of the lower and upper sidebands, respectively. The EOM is driven by a radio frequency (RF) signal with a varying frequency to perform a scan for reconstructing the Brillouin spectra over the FUT. In the receiver stage, the aforementioned OLO and SpBS light are mixed via Coupler2 and then detected by a balanced photodetector (BPD). The optical power entering Coupler2 and that reaching the BPD are approximately equal due to the negligible coupling loss and insertion loss of the Coupler2. The uncorrelated Stokes and Anti-Stokes signals beat with the lower and upper sidebands of OLO, respectively, resulting in an electrical signal in the distance domain merged with zero-mean additive noise attributed to various noise types, as exemplified by Fig. 1(a). Due to the use of balanced detection scheme, the impact of relative intensity noise from the laser is greatly mitigated and thus omitted in the analysis, and the photodetection noises including thermal and shot noises are mainly considered hereafter. The detailed mathematical process modelling the electrical signal and noise output from the BPD is addressed in Appendix A instead of here for brevity. The output of BPD then passes through an electrical bandpass filter (BPF) that selects the desired spectra of both signal and noise within its passband, giving rise to a response in the distance domain shown by Fig. 1(b), here designated as $V_b(z)$ that can be readily derived from (9A) in Appendix A and

TABLE I
EXPECTATION VALUES AND STDs OF THE THREE TERMS IN (4)

Terms	Expectation values	STDs
$\text{LPF}\{I_{b-s}^2(z)\}$	$\mu_{s^2}(z) = P_{Lo}P_S(z)/2$ (5)	$\sigma_{s^2}(z) = P_{Lo}P_S(z)/2$ (6)
$\text{LPF}\{2I_{b-s}(z)I_{b-n}(z)\}$	$\mu_{2sn}(z) = 0$ (7)	$\sigma_{2sn}(z) = \sqrt{P_{Lo}P_S(z)}\sigma_{b-n}$ (8)
$\text{LPF}\{I_{b-n}^2(z)\}$	$\mu_{n^2}(z) = \sigma_{b-n}^2$ (9)	$\sigma_{n^2}(z) = \sigma_{b-n}^2$ (10)

depicted as:

$$\begin{aligned}
 V_b(z) &\propto I_{b-s}(z) + I_{b-n}(z) \\
 &= R\sqrt{P_{Lo}P_S(z)}F[\Delta f(z)]\cos[\theta(z)] \\
 &\quad \cdot \{\cos[H(z) + \phi_1(z)] + \cos[H(z) + \phi_2(z)]\} \\
 &\quad + I_{b-n}(z) \quad (2)
 \end{aligned}$$

where $I_{b-s}(z)$ is the photocurrent of the beating signal output from the BPF; $R \approx 1 \text{ A/W}$ is the responsivity of the photodiode, which will be omitted in the following derivation process for brevity, and the resulting unit mismatch problem will also be ignored as it does not substantially affect the analysis; $\Delta f(z) = |f_{S1}(z) - f_{Lo1}| = |f_{S2}(z) - f_{Lo2}|$, $f_{S1}(z)$ and $f_{S2}(z)$ being the frequency of the Stokes and Anti-Stokes SpBS light at each fiber position z respectively, f_{Lo1} and f_{Lo2} being the frequency of the two OLO sidebands, respectively; $F[\Delta f(z)]$ is a normalized power coefficient representing how much power of Brillouin signal from the BPD passes through the BPF, which depends on the spectral position of the BPF passband and $\Delta f(z)$; the angle $\theta(z)$ is the local relative polarization rotation of the SpBS with respect to the OLO, varying in the range $[0, \pi/2]$; $H(z) = 4\pi\Delta f(z)Nz/c$ indicates the carrier phase of the beating signal; $\phi_1(z)$ (or $\phi_2(z)$) is the random phase difference between the Stokes (or Anti-Stokes) SpBS signal and the lower (or upper) OLO sideband reaching the BPD; $I_{b-n}(z)$ is the noise photocurrent at the BPF output, mainly attributed to filtered thermal noise and shot noise, and can be characterized by its standard deviation (STD) as [26]:

$$\begin{aligned}
 \sigma_{b-n}(z) &= \sqrt{\sigma_{b-th}^2 + \sigma_{b-sh}^2(z)} \\
 &= \sqrt{\sigma_T^2 B_F + 2q[P_{Lo} + P_S(z)]B_F} \\
 &\approx \sqrt{\sigma_T^2 B_F + 2qP_{Lo}B_F} \quad (3)
 \end{aligned}$$

where σ_{b-th} and $\sigma_{b-sh}(z)$ stand for the STDs of filtered thermal noise and shot noise, respectively; σ_T^2 is the power spectral density (PSD, in unit of A^2/Hz) of the thermal noise, which must be obtained experimentally by measuring the PD output voltage without light input [17]; $q = 1.6 \times 10^{-19} \text{ C}$ is the electron charge; B_F is the bandwidth of BPF, which typically equals to $1/D_p$. The approximation in (3) holds due to the fact that the rather weak $P_S(z)$ negligibly impacts on $\sigma_{b-sh}^2(z)$ with respect to the much stronger P_{Lo} in a heterodyne detection configuration.

The distance-domain envelope of $V_b(z)$, i.e., the response of port c , designated as $A_c(z)$, is then produced by an off-the-shelf envelope detector (ED), as shown by Fig. 1(c). The ED conducts essentially a power detection (square detection) process, which can therefore be mathematically depicted by firstly squaring $V_b(z)$ and then performing a low-pass filtering operation $\text{LPF}\{*\}$ with a bandwidth equal to $1/D_p$, yielding:

$$\begin{aligned}
 A_c(z) &= \text{LPF}\{V_b^2(z)\} \\
 &\propto \text{LPF}\{I_{b-s}^2(z)\} + \text{LPF}\{2I_{b-s}(z)I_{b-n}(z)\} \\
 &\quad + \text{LPF}\{I_{b-n}^2(z)\} \quad (4)
 \end{aligned}$$

This enables to mathematically model the local SNR of $A_c(z)$ by comprehensively analyzing the last three terms of (4). In the analysis we rationally assume $F[\Delta f(z)] \approx 1$ such that omitting $F[\Delta f(z)]$ in the following equations for simplicity and visual clarity, since by definition $SNR(z)$ is the SNR at the peak-value frequency of the Brillouin spectrum at each fiber position z [16], in which case most power of the local Brillouin spectrum passes through the BPF. By substituting (2) into (4), the statistic parameters - the expectation value and STD - of each term at each fiber position z , are derived as summarized in Table I (see detailed derivation in Appendix B).

From Table I it can be observed that the expectation of $A_c(z)$ (i.e., the noiseless envelope trace) is simply the summation of a signal term expressed by (5) and a constant bias expressed by (9). The trivial latter can practically be removed in actual measurement by subtracting the measured data by the mean value of its direct current part. On the other hand, Table I indicates that the power detection process makes the measurement affected by three types of noises: I) the polarization noise, i.e., the randomly varying polarization fading effect resulting from the beating between the OLO light and the PSc-induced randomly polarized SpBS light (the mechanism is similar to the polarization noise in the BOTDA sensors based on PSc [18]), II) the signal-amplified detection noise, and III) the squared detection noise, with STDs denoted by (6), (8) and (10), respectively. Based on these signal and noise terms, the SNR at each position z along the FUT under M times trace (i.e., $A_c(z)$) averaging can be represented as:

$$SNR(z) = \frac{\mu_{s^2}(z)\sqrt{M}}{\sqrt{\sigma_{s^2}^2(z) + \sigma_{2sn}^2(z) + \sigma_{n^2}^2(z)}} \quad (11)$$

This SNR model constitutes a theoretical tool to anticipate the performance of FS-BOTDR under a given measurement condition, by readily substituting system parameters into (11).

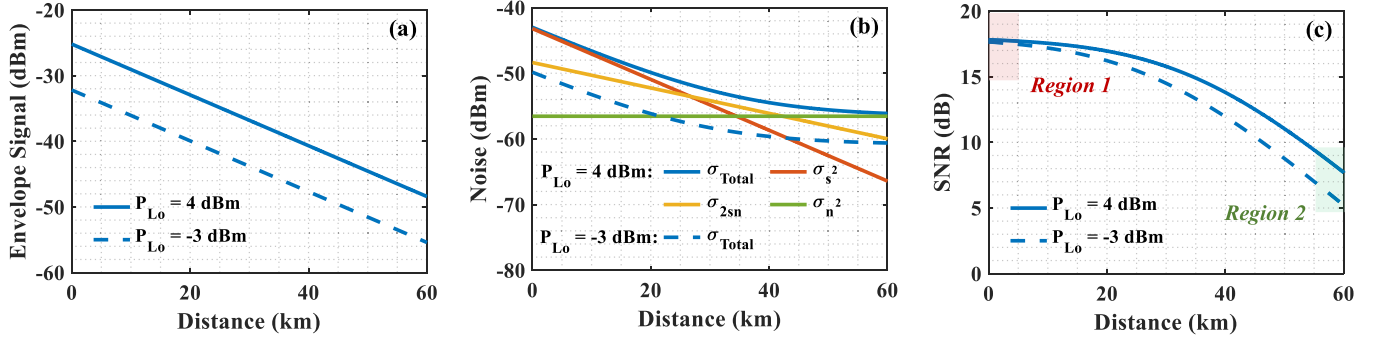


Fig. 2. Calculation results with distinct OLO powers based on (11); (a) Envelope signal profiles; (b) Noise profiles; (c) SNR profiles. Simulation's parameters are: $n = 1.44$, $k_S = 3 \times 10^{-10}$ /m, $c = 3 \times 10^8$ m/s, $\sigma_T^2 = 2 \times 10^{-22}$ A²/Hz, $R = 1$ A/W, $F[\Delta f(z)] = 0.92$, $\alpha = 0.2$ dB/km, $P_p = 25$ dBm, $D_p = 50$ ns, $B_F = 20$ MHz, $z_{\max} = 60$ km, $P_{L_o} = 4$ dBm, $M = 4000$.

More importantly, the model also enables to comprehensively understand the SNR behavior and optimize system parameters of standard FS-BOTDR. For instance, considering a typical measurement scenario with 5 m spatial resolution and 60 km sensing range, the theoretically anticipated signal, noise and SNR trends calculated from (11), respectively, are shown by solid curves in Fig. 2(a)–2(c) with logarithmic scale, where $\sigma_{Total}(z) = \sqrt{\sigma_{s^2}^2(z) + \sigma_{2sn}^2(z) + \sigma_{n^2}^2(z)}$. It can be observed that the signal decays linearly (i.e., exponentially in linear scale) with distance as affected by the intrinsic fiber loss (solid curve in Fig. 2(a)), whilst the noise shows an uneven trend (solid blue curve in Fig. 2(b)), giving rise to a SNR trend not always linear with the signal power (solid curve in Fig. 2(c)). This is essentially attributed to the signal-dependent noises, i.e., polarization noise (red) and signal-amplified detection noise (yellow), both decaying with distance, superpose on the evenly distributed squared detection noise (green). This way the polarization noise dominates at the fiber near-end and decays faster than the signal-amplified noise; at the fiber far-end, the squared detection noise turns dominating. On the other hand, by adjusting the OLO power from 4 dBm to -3 dBm while keeping other parameters unchanged, both signal and noise decrease accordingly with distinct behaviors (dashed curves in Fig. 2(a) and 2(b), for visual clarity in Fig. 2(b) only the trend of total noise is illustrated), resulting in a SNR trend shown by the dashed curve in Fig. 2(c). It can be found that such a SNR curve is not entirely down-shifted with respect to that with the OLO power of 4 dBm, rather they interestingly show a similar SNR level at the fiber near-end. All analysis above indicates that the SNR feature of FS-BOTDR is distance-dependent, which can be further elaborated by observing the typical regions of the FUT as:

- I) *Region 1* (light red in Fig. 2(c)): typically corresponding to the fiber positions around the fiber near-end of a long FUT, or over the entire fiber length of a short FUT, where the polarization noise dominates, which is here designated as polarization-noise-limit condition. In this region (11) can be simplified to (the detailed mathematical derivation is shown from (1C)–(5C) in Appendix C):

$$SNR(z) \approx \sqrt{M}, \quad \text{for } P_{L_o}[P_S(z) - 8qB_F] \gg 4\sigma_T^2 B_F \quad (12)$$

M being the number of trace averaging. In this case the SNR can approach an upper limit of \sqrt{M} as long as P_{L_o} is sufficiently large (guaranteed by the condition term in (12)) to make the contribution of (8) and (10) far smaller than that of (6). Note that, since (6) grows much faster than (8) and (10) as P_{L_o} increases, the minimum required P_{L_o} to reach such a polarization-noise-limit condition (~ -8 dBm as calculated based on the condition term in (12)) is smaller than that of conventional shot-noise-limit condition. This essentially explains why the achieved SNR is similar when using 4 dBm and -3 dBm OLO powers (both beyond the minimum required value to approach the upper limit of \sqrt{M}).

- II) *Region 2* (light green in Fig. 2(c)): typically corresponding to the fiber positions around the fiber far-end of a long FUT, where the square detection noise dominates. In this region (11) can be rewritten as (the detailed mathematical derivation is shown from (6C)–(9C) in Appendix C):

$$SNR(z) \approx \frac{\sqrt{M}P_S(z)}{4qB_F}, \quad \text{for } P_{L_o} \gg \frac{\sigma_T^2}{2q} \quad (13)$$

which corresponds to the conventional shot-noise-limit condition, and can be reached as long as P_{L_o} is sufficiently large (guaranteed by the condition term in (13), calculated as ~ 7 dBm) to make the thermal noise far smaller than the shot noise. In this case the SNR turns linearly proportional to the signal power $P_S(z)$ that is concretely expressed by (1).

From above two typical cases it can be noticed that the optimization of P_{L_o} can be theoretically realized based on (11), which depends on measurement conditions, being distinguished from the routine of taking the maximum possible power that is just below the PD saturation all the time, as will be further experimentally verified in Section III.

III. EXPERIMENTAL VERIFICATION AND DISCUSSION

A standard FS-BOTDR system shown by Fig. 1 has been implemented for experimental validation. To demonstrate the generality of the SNR model, both long-rang (~ 50 km-long FUT) and short range (~ 5 km-long FUT) sensing scenarios are

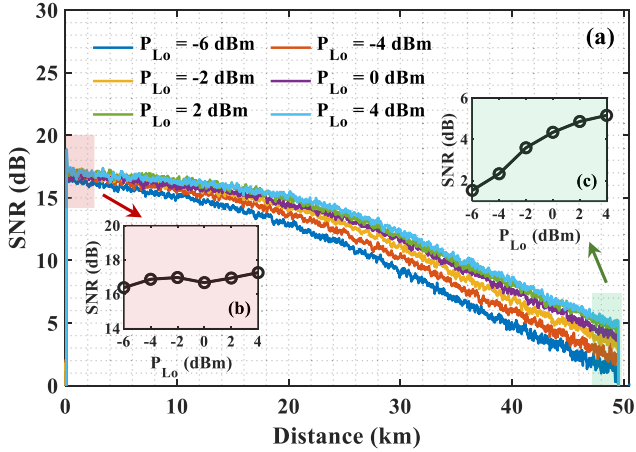


Fig. 3. SNR behaviors under different OLO powers. (a) SNR profiles along the ~ 50 -km long FUT with 2-m spatial resolution. (b) SNR at 50-km fiber near-end as a function of OLO power. (c) SNR at 50-km fiber far-end as a function of OLO power.

investigated. In each scenario, experiments are carried out with spatial resolutions of 1 m, 2 m and 6 m, corresponding to pulse durations of 10 ns, 20 ns and 60 ns, respectively. The bandwidths of BPFs are chosen as 100 MHz, 50 MHz and 17 MHz to match the spatial resolutions used, respectively. Since aiming to investigate the SNR behavior, for which only the envelope trace corresponding to the peak-value frequency of Brillouin spectra (i.e., near BFS) is required, therefore in the experiment the RF signal is not scanned, rather it is delicately set to guarantee that most $\Delta f(z)$ are spectrally located around the central frequency of the BPF, i.e., $F[\Delta f(z)] \approx 1$. A 400-MHz BPD is used in the experiment, the thermal noise PSD of which is measured experimentally as $\sigma_T^2 \approx 1.97 \times 10^{-22} \text{ A}^2/\text{Hz}$ [17]. For each spatial resolution, the envelope signal output from the ED is acquired with 4000 times trace averaging to ensure a decent SNR for the sake of visual clarity. The measurement is consecutively repeated by several times under the same experimental condition, from which the experimental SNR can be achieved by taking the ratio between the mean values of the repeated traces (i.e., experimentally obtained signal) and their STDs (i.e., experimentally obtained noise) at each fiber position.

A. Long-Distance Sensing Scenario (~ 50 Km-Long FUT)

Experiments for the long-distance sensing scenario are carried out with a ~ 50 km-long FUT. Based on (13) that indicates a linear dependence between $P_S(z)$ and SNR in the long-distance scenario, the peak power of the incident optical pulse, P_p , is maximized to ~ 25 dBm, being exactly below the threshold of modulation instability (MI) [27], to maximize $P_S(z = 50 \text{ km})$ so as to maximize the SNR. According to the condition term in (13), P_{Lo} is set to the largest possible value of ~ 4 dBm (measured at the input of Coupler2, as limited by the optical power budget of the experimental system) to approach the shot-noise-limit condition for all spatial resolutions used. This procedure is verified by Fig. 3(a) that experimentally compares SNR profiles along the ~ 50 km-long FUT with 2-m spatial resolution, under different P_{Lo} changing from -6 dBm to 4 dBm at an interval of 2 dB. In

the figure all SNR profiles show nonlinearly decaying trends, matching with the theoretical anticipation as illustrated by Fig. 2(c). Furthermore, around the fiber near-end corresponding to *Region 1* in Section II, it is verified that the SNR remains almost unchanged and close to the upper limit \sqrt{M} ($\sqrt{4000}$, ~ 18 dB in the logarithmic scale), as more clearly illustrated in Fig. 3(b), due to fact that all P_{Lo} used are close to or larger than the minimum value satisfying the condition term of (12). It is normal that with a spatial resolution of 2 m, the SNR does not completely reach the theoretical upper limit, because precisely speaking, the signal-amplified noise (8) is not completely negligible, so that the polarization noise (6) does not completely dominate even if P_{Lo} is sufficiently large. In principle, the wider the spatial resolution, the larger the P_S , the more dominant the polarization noise, and the closer the SNR is to the upper limit. On the other hand, at the fiber far-end corresponding to *Region 2* in Section II, the SNR is as expected maximized at the highest P_{Lo} as shown in Fig. 3(c), since all P_{Lo} used are smaller than the minimum required value of ~ 7 dBm that satisfies the condition term of (13).

With the system parameters set above, the correctness of theoretically anticipated signal, noise and SNR curves are respectively investigated by comparing with experimental results. Fig. 4(a)–4(c) show the experimental acquired envelope signals (light blue curves) with distinct spatial resolutions of 1 m, 2 m, and 6 m, respectively, all in logarithmic scale and being greatly consistent with the theoretical anticipations (dark blue curves) calculated from (5). The noise behavior is then investigated, characterized by the STD of the envelope signal at each fiber position computed from the repeating measurements, as shown by the light blue curves with logarithmic scale in Fig. 4(d)–4(f) for distinct spatial resolutions. In the figures the theoretically derived STDs of distinct noise sources (red, yellow and green curves) and the total noise (dark blue curves) at each fiber position are also illustrated for comparison, the latter showing a good agreement with experimental results (light blue curves). It can be found that for all spatial resolutions the signal-dependent polarization noise indicated by (6) and the signal-amplified detection noise (mainly shot noise) indicated by (8) dominate at the fiber near-end; the wider the spatial resolution, the more domination of the polarization noise as it is linearly proportional to the signal power. Signal-dependent noises decay along the fiber, such that at the fiber far-end the total noise is more determined by the signal-independent squared shot noise indicated by (10); the narrower the spatial resolution, the more domination of the squared shot noise. The SNR at each fiber position for distinct spatial resolutions is shown by the light blue curves in Fig. 4(g)–4(i), respectively, all matching well with the theoretical curves (dark blue) anticipated based on (11), verifying the accuracy and generality of the proposed SNR model.

B. Short-Distance Sensing Scenario (~ 5 Km-Long FUT)

The SNR in short-range sensing scenario, expected to behave as stated by *Region 1* in Section II, is here experimentally investigated with a ~ 5 km-long FUT. Based on analysis in Section II, in such a short-range sensing scenario the OLO power

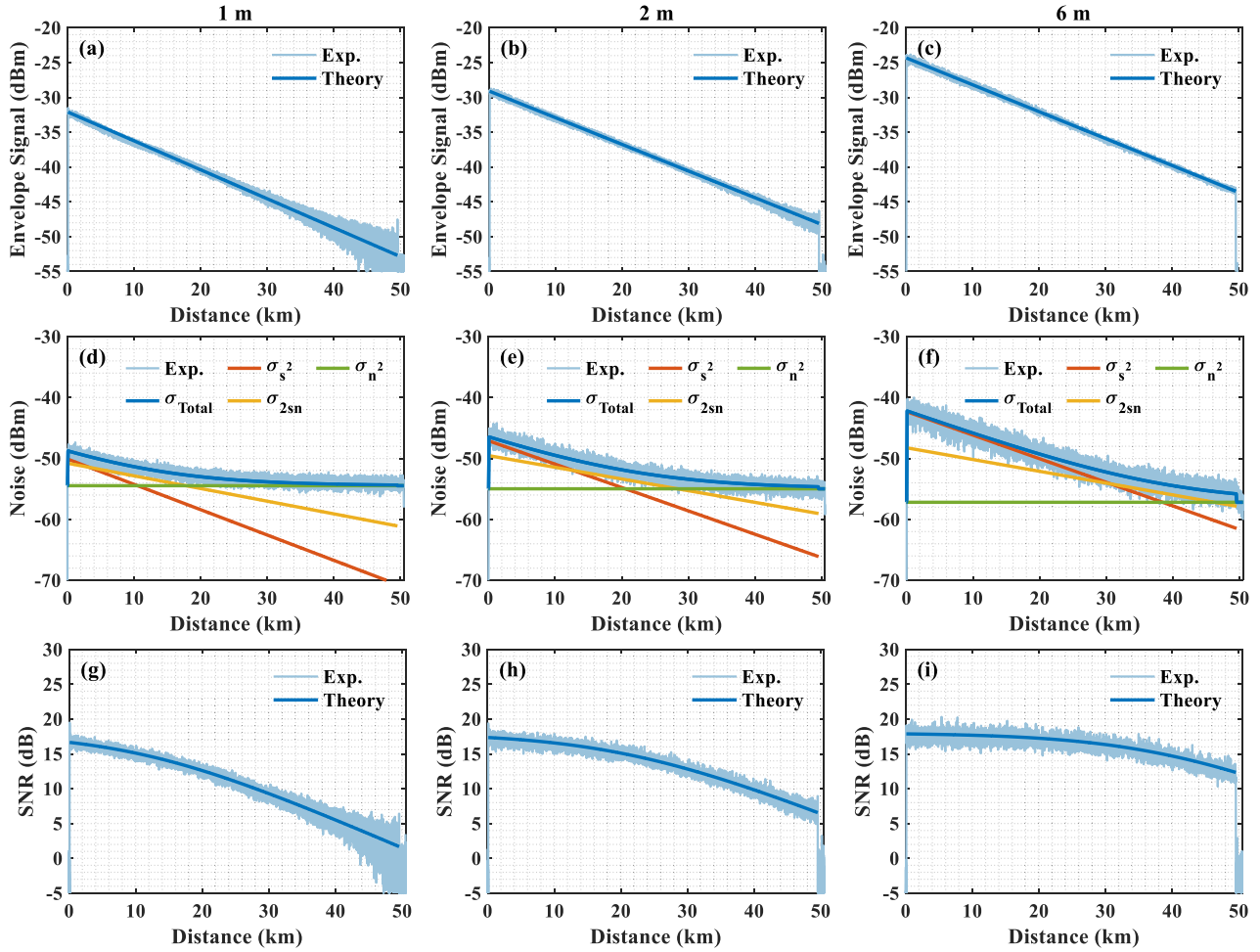


Fig. 4. Comparison of theoretical and experimental results along a ~ 50 km-long FUT; (a), (b), (c): Envelope signals with spatial resolutions of 1 m, 2 m, and 6 m, respectively; (d), (e), (f): STDs of distinct noises with spatial resolutions of 1 m, 2 m, and 6 m, respectively; (g), (h), (i): SNR profiles with spatial resolutions of 1 m, 2 m, and 6 m, respectively.

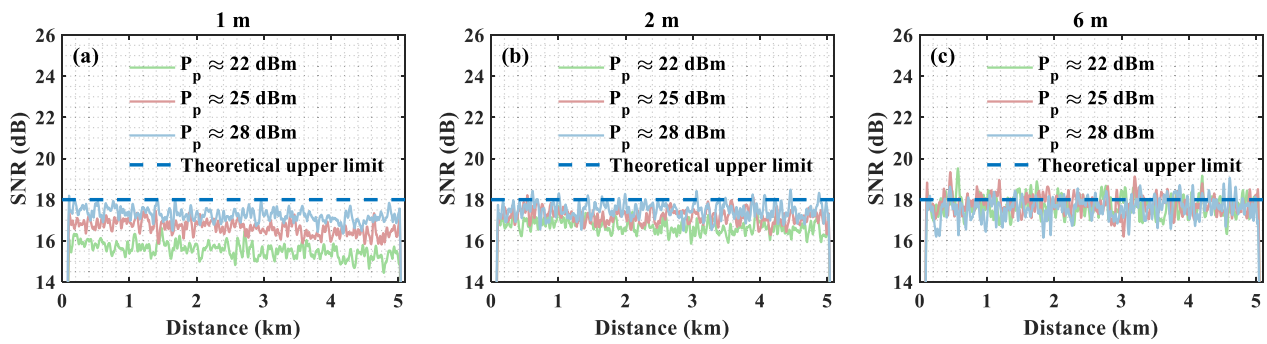


Fig. 5. SNR profiles along a ~ 5 -km long FUT measured at distinct pulse peak powers with spatial resolutions of: (a) 1 m; (b) 2 m; and (c) 6 m.

P_{Lo} and input pulse peak power P_p are no longer independently optimized as is the case for the long-sensing range scenario, but should be jointly optimized based on the condition term of (12). It means that the optimized power of P_{Lo} and P_p may not have to be their respective largest possible values. Indeed, Fig. 3(b) has already demonstrated that any P_{Lo} greater than ~ -9 dBm, though much lower than the largest possible value of ~ 4 dBm, can result in a similar SNR close to the upper limit \sqrt{M} (here

~ 18 dB). And vice versa, such an upper limit SNR can alternatively be achieved by combining a sufficiently high P_{Lo} with a P_p much lower than its largest possible value (limited by fiber nonlinear effects such as MI, here ~ 31 dBm for the 5-km long FUT [27]). To demonstrate this deduction, SNR trends along the FUT are experimentally measured at distinct pulse peak power P_p under a fixed P_{Lo} of ~ 4 dBm, with spatial resolutions of 1 m, 2 m and 6 m, as shown by Fig. 5(a)–(c), respectively. It can

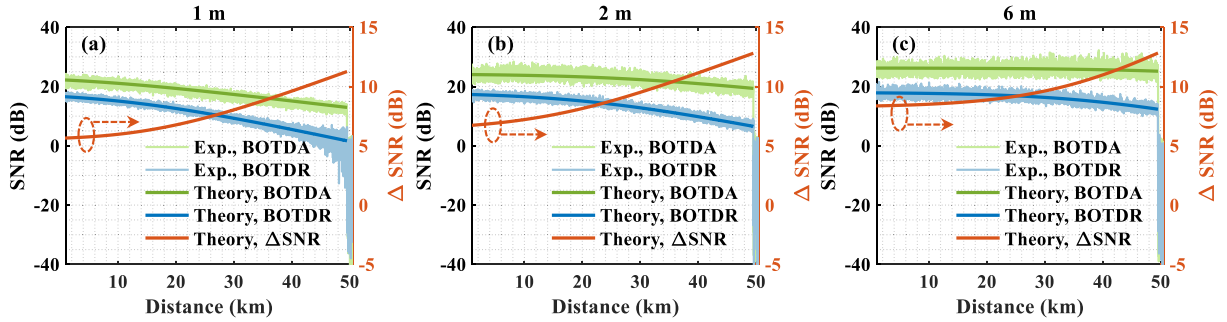


Fig. 6. SNR behaviors of BOTDA and FS-BOTDR along a ~50 km-long FUT with spatial resolutions of: (a) 1 m; (b) 2 m; and (c) 6 m.

be observed that, the SNR is improved with the increase of P_p in the case of 1 m spatial resolution, since all used pulse peak power are not sufficiently high to satisfy the condition term of (12), i.e., to satisfy $P_p > 28.5$ dBm (see detailed calculation in Appendix D); on the other hand, in cases of 2 m and 6 m spatial resolutions, the SNR remains similar with any P_p used, since all used pulse peak power could satisfy the condition term of (12) ($P_p > 22.5$ dBm for 2 m spatial resolution and $P_p > 13.0$ dBm for 6 m spatial resolution, see detailed calculation in Appendix D). From Fig. 5 it can be also clearly observed that, the SNR with wider spatial resolution is closer to the theoretical upper limit, due to a more dominating polarization noise expressed by (6) (i.e., a more negligible signal-amplified noise expressed by (8)). However, it is important to note that, even though the SNR has been saturated (e.g., all SNR curves overlap in the case of 6 m spatial resolution), the saturated SNR level is still slightly lower than the theoretical upper limit (less than 1 dB), implying that there might be other sources of noise affecting the SNR behaviour. In this work, we do not study this point in more detail, because the suspected additional noise does not tangibly impact on the SNR analysis at least for PSc-based FS-BOTDR. All above mentioned results demonstrate the correctness of the theoretical analysis regarding *Region 1* in Section II, which offers a guideline optimizing OLO power and pulse peak power towards a minimum energy consumption of the system.

C. Quantitative Comparison of SNR Between FS-BOTDR and BOTDA

Combining the here proposed SNR model of FS-BOTDR and the existing SNR model of BOTDA in literature [17], [18], [19] makes it possible to theoretically quantify the SNR difference between the two techniques under the same measurement condition. In this section, for fair comparison, the identical system parameters including peak pulse power, spatial resolutions, length of FUT, number of trace averaging, frequency scanning step, and the same experimental devices except for BPF and ED, as used in the experiment of FS-BOTDR conducted in Section III-A, are adopted to build up an optimized standard long-range BOTDA with a Brillouin loss configuration and a direct detection scheme with pre-amplification as described in [17], [28]. The noise sources of BOTDA system used in this section routinely includes polarization noise, photo-detection noise,

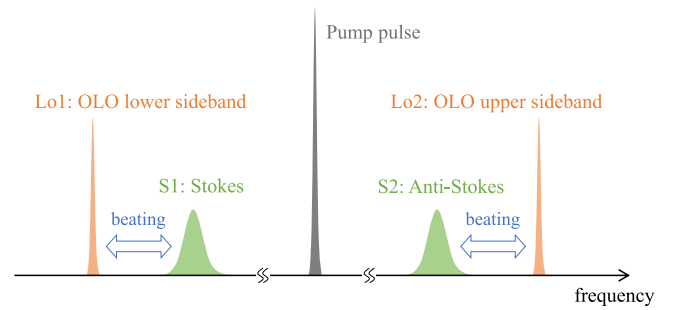


Fig. 7. Schematic diagram of the beating process between SpBS and OLO.

signal-SpBS beating noise and signal-ASE beating noise [17], [18], [19].

Fig. 6(a)–6(c) show the theoretically anticipated and experimentally obtained SNR results of optimized BOTDA (green curves) and BOTDR (blue curves, reused from Section III-A) with spatial resolutions of 1 m, 2 m, and 6 m, respectively, where the experimental SNR profiles of BOTDA (light green curves) are in perfect agreement with the theoretical calculations (dark green curves) based on [17], [18], [19]. It can be seen that, with any spatial resolution used, the SNR of BOTDR is always weaker than that of BOTDA, in consistent with the general cognition in the Brillouin sensing community. It can be further observed that their SNR difference (denominated by ΔSNR) shown by red curves with right-hand vertical axis in Fig. 6, grows gradually, whether along the FUT or with the expands of spatial resolution. More specifically, at the 50-km fiber far end, the SNR of BOTDA is around 10 dB higher than that of BOTDR (the SNR of BOTDA is ~11 dB, ~12 dB, ~13 dB larger than that of BOTDR with spatial resolutions of 1 m, 2 m, 6 m, respectively). Results highlight that the SNR difference between the two Brillouin-based time-domain systems under any given system parameters can be theoretically anticipated, thanks to the here proposed SNR model of FS-BOTDR.

IV. CONCLUSION

In this study, an accurate SNR model of standard FS-BOTDR, covering the procedure from the photodetection process to the envelope detection process, considering all signal and noise terms with substantial impact on sensing performance, has been established for the first time to the best of our knowledge. The accuracy and generality of the established SNR model have been

experimentally validated by excellent quantitative agreement between theory and measurement under various experimental conditions. The proposed SNR model serves as a theoretical tool, paving the way to efficiently design and evaluate a FS-BOTDR system in terms of:

- 1) precisely anticipating the SNR performance of FS-BOTDR under any given measurement condition, with no need to build experimental setup or carry out experiments. The anticipation only requires the system parameters present in (1) and (11) such as fiber length, optical pulse width, optical pulse peak power, and so on.
- 2) comprehensively understanding the SNR behavior of FS-BOTDR system. The model clarifies the quantitative relation between the signal and each type of noise. It points out that signal-dependent noises, mainly including polarization noise and signal-amplified detection noise, which have not been adequately addressed in previous literature, in fact impact significantly on the system performance. This enables to precisely interpret for the first time the nonlinear dependence of the SNR profile on the signal power. The model also brings on an essential novel finding that there exists an upper limit of SNR equal to \sqrt{M} , M being the number of envelope trace averaging, which can be approached at the fiber positions where the signal power is sufficiently large such that the signal-dependent polarization noise is absolutely dominant.
- 3) theoretically quantifying the SNR difference between FS-BOTDR and standard BOTDA by combining the existing SNR model of BOTDA in literature [17], [18], [19]. Under the same measurement condition, it is found out that the SNR differences between the two techniques grow gradually with the increase of spatial resolution and fiber distance. Taking 50 km-long sensing distance as an example, it has been verified that the SNR of FS-BOTDA at the fiber far-end is in the order of 10 dB higher than that of FS-BOTDR with meter-scale spatial resolutions.
- 4) guiding the optimization of system parameters towards the highest possible SNR with minimized energy consumption. It is pointed out that in some scenarios, e.g., with short-range FUT, the OLO power and optical pulse peak power should be jointly optimized, and the optimized powers may be much lower than the largest possible values. Using any power higher than the optimum value brings tiny benefit to the system performance, and the latter is obviously more preferable from the perspective of energy conservation.

It is interesting to note that, if the SNR upper limit highlighted in this work is solely attributed to the polarization noise caused by the polarization scrambler, the limit may be overcome by using other interrogation schemes without the polarization noise. These schemes include but are not limited to those based on a polarization switch or a polarization diversity coherent receiver. However, this perspective may not be entirely valid, as we have noticed from Fig. 5 and briefly commented in Section III-B that the realistic upper limit of SNR might be affected by other sources of noise, which we will study in more detail in the near future.

On the other hand, further study may also focus on addressing the SNR model of other BOTDR approaches, for instance the one directly performing short-time Fourier transform on the beating signal [6], [7], [8], to enrich the fundamental understanding on various Brillouin-based time-domain distributed optical fiber sensors. This may help to select the appropriate sensors for technicians facing different application requirements, without the need of conducting sophisticated experiments.

APPENDIX A

This appendix shows the detailed mathematical derivations for modelling the electrical signal output from the BPD in Section II (i.e., the signal at port a in Fig. 1). The electrical signal results from the beating of the Stokes SpBS and the lower OLO sideband, and that of the Anti-Stokes SpBS and the upper OLO sideband, as shown in Fig. 7. The field amplitudes of the Stokes and Anti-Stokes light, designated as $\vec{E}_{S1}(t)$ and $\vec{E}_{S2}(t)$, respectively, can be described as:

$$\vec{E}_{S1}(t) = \{ \hat{x} \cos[\theta(t)] e^{j\phi_{S1}^x(t)} + \hat{y} \sin[\theta(t)] e^{j\phi_{S1}^y(t)} \} \cdot E_{S1}(t) e^{j2\pi f_{S1}(t)t} \quad (1A)$$

$$\vec{E}_{S2}(t) = \{ \hat{x} \cos[\theta(t)] e^{j\phi_{S2}^x(t)} + \hat{y} \sin[\theta(t)] e^{j\phi_{S2}^y(t)} \} \cdot E_{S2}(t) e^{j2\pi f_{S2}(t)t} \quad (2A)$$

where \hat{x} and \hat{y} stand for the polarization direction of the OLO light and its orthogonal direction, respectively; the angle $\theta(t)$ is the local relative polarization rotation of the SpBS with respect to the OLO, varying in the range $[0, \pi/2]$; $\phi_{S1}^x(t)$, $\phi_{S1}^y(t)$, $\phi_{S2}^x(t)$, and $\phi_{S2}^y(t)$ are the random phase differences in \hat{x} and \hat{y} polarization direction between the SpBS signal and OLO light reaching the input of Coupler2; $E_{S1}(t)$ and $E_{S2}(t)$ are the optical amplitudes of the Stokes and Anti-Stokes waves respectively; j is an imaginary unit; $f_{S1}(t)$ and $f_{S2}(t)$ represent the local frequency of the Stokes and Anti-Stokes waves, respectively.

The lower and upper sidebands of OLO wave reaching the input of Coupler2, designated as $\vec{E}_{Lo1}(t)$ and $\vec{E}_{Lo2}(t)$, respectively, can be described as:

$$\vec{E}_{Lo1}(t) = \hat{x} E_{Lo1}(t) e^{j2\pi f_{Lo1}t} \quad (3A)$$

$$\vec{E}_{Lo2}(t) = \hat{x} E_{Lo2}(t) e^{j2\pi f_{Lo2}t} \quad (4A)$$

where $E_{Lo1}(t)$ and $E_{Lo2}(t)$ are the field amplitudes of each sideband of OLO wave; f_{Lo1} and f_{Lo2} represent the frequency of each OLO sideband, respectively.

According to the optical transfer function of the 2×2 optical coupler with 50:50 splitting ratio (power-coupling coefficient $\varepsilon = 0.5$), the field amplitudes of the composed optical signal at two outputs of Coupler2 can be depicted as [29]:

$$\begin{aligned} \begin{bmatrix} \vec{E}_{C1}(t) \\ \vec{E}_{C2}(t) \end{bmatrix} &= \begin{bmatrix} \sqrt{1-\varepsilon} & j\sqrt{\varepsilon} \\ j\sqrt{\varepsilon} & \sqrt{1-\varepsilon} \end{bmatrix} \begin{bmatrix} \vec{E}_{S1}(t) + \vec{E}_{S2}(t) \\ \vec{E}_{Lo1}(t) + \vec{E}_{Lo2}(t) \end{bmatrix} \\ &= \begin{bmatrix} \frac{1}{\sqrt{2}} & j\frac{1}{\sqrt{2}} \\ j\frac{1}{\sqrt{2}} & \frac{1}{\sqrt{2}} \end{bmatrix} \begin{bmatrix} \vec{E}_{S1}(t) + \vec{E}_{S2}(t) \\ \vec{E}_{Lo1}(t) + \vec{E}_{Lo2}(t) \end{bmatrix} \end{aligned} \quad (5A)$$

The SpBS light including Stokes and Anti-Stokes lines beats with double-sideband OLO light in a BPD, where the upper beating frequency components (e.g., originating from the beating process between $\overrightarrow{E_{S1}}(t)$ and $\overrightarrow{E_{Lo2}}(t)$, ~ 20 GHz) are filtered out by the BPD with a bandwidth of a few hundred megahertz. This way the optical power of the composed optical signal reaching two inputs of the BPD can be expressed as:

$$P_1(t) \propto \text{LPF}_{\text{BPD}} \left\{ \overrightarrow{E_{C1}}(t) \overrightarrow{E_{C1}}^*(t) \right\} \quad (6A)$$

$$P_2(t) \propto \text{LPF}_{\text{BPD}} \left\{ \overrightarrow{E_{C2}}(t) \overrightarrow{E_{C2}}^*(t) \right\} \quad (7A)$$

where $\text{LPF}_{\text{BPD}}\{*\}$ represents the filtering operation from the BPD; $\overrightarrow{E_{C1}}^*(t)$ and $\overrightarrow{E_{C1}}(t)$ represent the complex conjugate of $\overrightarrow{E_{C1}}(t)$ and $\overrightarrow{E_{C1}}(t)$, respectively.

The output of BPD, i.e., the response of port a , consisting of the differential signal between two electrical signals corresponding to two inputs of BPD and inevitable zero-mean additive noise mainly attributed to the photo-detection process, can be converted into the distance domain using the the mode group velocity in vacuum c , and expressed as:

$$\begin{aligned} V_a(z) &\propto I_{a-s}(z) + I_{a-n}(z) = RP_1(z) - RP_2(z) + I_{a-n}(z) \\ &= 2R\sqrt{P_{Lo1}P_{S1}(z)}\cos[\theta(z)]\cos[H(z) + \phi_1(z)] \\ &\quad + 2R\sqrt{P_{Lo2}P_{S2}(z)}\cos[\theta(z)]\cos[H(z) + \phi_2(z)] \\ &\quad + I_{a-n}(z) \end{aligned} \quad (8A)$$

where $H(z) = 4\pi\Delta f(z)Nz/c$; $\Delta f(z) = |f_{S1}(z) - f_{Lo1}| = |f_{S2}(z) - f_{Lo2}|$; P_{Lo1} and P_{Lo2} are the power of the lower and upper OLO sideband, respectively, and $P_{Lo1} = P_{Lo2}$; $P_{S1}(z)$ and $P_{S2}(z)$ are the powers of the Stokes and Anti-Stokes SpBS signal, respectively, and $P_{S1}(z) = P_{S2}(z)$; $I_{a-s}(z)$ is the photocurrent of the beating signal output from BPD; $R \approx 1$ A/W is the responsivity of the photodiode, which will be omitted in the following derivation process for brevity, and the resulting unit mismatch problem will also be ignored as it does not substantially affect the analysis; N is the effective group index of the propagating mode in the fiber; $\phi_1(z) = \phi_{S1}^x(z) - \pi/2$ and $\phi_2(z) = \phi_{S2}^x(z) - \pi/2$, are the random phase difference between the SpBS signal and OLO reaching the BPD. Considering the total SpBS power $P_S(z) = P_{S1}(z) + P_{S2}(z)$ and total OLO power $P_{Lo} = P_{Lo1} + P_{Lo2}$, (8A) can be simplified to:

$$\begin{aligned} V_a(z) &\propto R\sqrt{P_{Lo}P_S(z)}\cos[\theta(z)] \\ &\quad \cdot \{\cos[H(z) + \phi_1(z)] + \cos[H(z) + \phi_2(z)]\} \\ &\quad + I_{a-n}(z) \end{aligned} \quad (9A)$$

where $I_{a-n}(z)$ is the noise photocurrent, which usually composed of thermal and shot noises given that the relative intensity noise of the laser is greatly mitigated by the balanced detection scheme, and thus can be characterized by STD as:

$$\begin{aligned} \sigma_{a-n}(z) &= \sqrt{\sigma_{a-th}^2 + \sigma_{a-sh}^2} \\ &= \sqrt{\sigma_T^2 B_{PD} + 2q[P_{Lo} + P_S(z)]B_{PD}} \end{aligned}$$

$$\approx \sqrt{\sigma_T^2 B_{PD} + 2qP_{Lo}B_{PD}} \quad (10A)$$

where σ_{a-th} and $\sigma_{a-sh}(z)$ are the STDs of the total thermal noise and shot noise at port a , respectively; σ_T^2 is the PSD of the total thermal noise; $q = 1.6 \times 10^{-19}$ C is the electron charge; B_{PD} is the bandwidth of BPD. The approximation holds due to the fact that $P_S(z)$ has a negligible effect on shot noise with respect to the much larger P_{Lo} in a heterodyne detection configuration.

APPENDIX B

This appendix shows the detailed mathematical derivations of the results listed in Table I of Section II. The output of BPD shown by (9A) is selected by an electrical BPF and processed by an off-the-shelf ED, giving rise to the response of port b and c in succession, and then the expression of (2)–(4) in Section II can be obtained. The SNR model of the envelope signal $A_c(z)$, defined by the ratio of its expectation value and STD, can be established by characterizing the SNR of the three terms on the right-hand side of (4). The deriving process is briefly presented as following, in which we let $F[\Delta f(z)] \approx 1$, since by definition $SNR(z)$ is the SNR at the peak-value frequency of the Brillouin spectrum at each fiber position z [16], corresponding to the case that nearly all Brillouin information passes through the BPF.

1) The term of $\text{LPF}\{I_{b-s}^2(z)\}$ in (4).

By substituting (2) into the first term on the right-hand side of (4), the square term can be expressed as:

$$\begin{aligned} &\text{LPF}\{I_{b-s}^2(z)\} \\ &= P_{Lo}P_S(z)\cos^2[\theta(z)]\{1 + \cos[\Delta\phi(z)]\} \end{aligned} \quad (1B)$$

where $\Delta\phi(z) = \phi_1(z) - \phi_2(z)$, and $\cos^2[\theta(z)]$ varies between 0 and 1 following a uniform distribution with the number of measurements, which has been experimentally verified based on standard interferometry reflecting the state of polarization of the input light signal [29]. Note that the terms containing $\cos[2H(z)]$ signify the high frequency components (a few hundred megahertz and higher than $1/D_p$), which are filtered out during calculation by the operator $\text{LPF}\{*\}$ with a bandwidth equal to $1/D_p$.

Considering that $\cos^2[\theta(z)]$ follows a uniform distribution between 0 and 1, and $\phi_1(z)$ and $\phi_2(z)$ follow a uniform distribution between 0 and 2π , it can be obtained that $\overline{\cos^2[\theta(z)]} = 1/2$ and $\overline{\cos[\Delta\phi(z)]} = 0$. Thus the expectation value and STD of $\text{LPF}\{I_{b-s}^2(z)\}$, designated as $\mu_{s^2}(z)$ and $\sigma_{s^2}(z)$, respectively, can be calculated according to respective statistic definition:

$$\mu_{s^2}(z) = \overline{\text{LPF}\{I_{b-s}^2(z)\}} = \frac{P_{Lo}P_S(z)}{2} \quad (2B)$$

$$\begin{aligned} \sigma_{s^2}(z) &= \sqrt{\overline{\text{LPF}^2\{I_{b-s}^2(z)\}} - \mu_{s^2}^2(z)} \\ &= \frac{P_{Lo}P_S(z)}{2} \end{aligned} \quad (3B)$$

2) The term of $\text{LPF}\{2I_{b-s}(z)I_{b-n}(z)\}$ in (4).

Since the BPF bandwidth is less than the system acquisition bandwidth, $I_{b-n}(z)$ can be considered as a narrowband random

noise, which can be decomposed into in-phase and quadrature components [30]:

$$I_{b-n}(z) = I_{b-n}^I(z)\cos[H(z)] - I_{b-n}^Q(z)\sin[H(z)] \quad (4B)$$

where $I_{b-n}^I(z)$ and $I_{b-n}^Q(z)$ stand for the in-phase and quadrature components of $I_{b-n}(z)$, respectively. Such two independent components both follow zero-mean normal distributions with the same variance as $I_{b-n}(z)$. Thus, substituting (2) and (4B) into the second term on the right-hand side of (4), the cross term can be expressed as:

$$\begin{aligned} & \text{LPF}\{2I_{b-s}(z)I_{b-n}(z)\} \\ &= \sqrt{P_{Lo}P_S(z)}\cos[\theta(z)] \\ & \cdot \{I_{b-n}^I(z)\cos[\phi_1(z)] + I_{b-n}^I(z)\cos[\phi_2(z)] \\ & \quad + I_{b-n}^Q(z)\sin[\phi_1(z)] + I_{b-n}^Q(z)\sin[\phi_2(z)]\} \quad (5B) \end{aligned}$$

Since $\phi_1(z)$ and $\phi_2(z)$ follow a uniform distribution between 0 and 2π , the expectation value and STD of $\text{LPF}\{2I_{b-s}(z)I_{b-n}(z)\}$, designated as $\mu_{2sn}(z)$ and $\sigma_{2sn}(z)$, respectively, can be calculated according to their respective statistic definition:

$$\mu_{2sn}(z) = \overline{\text{LPF}\{2I_{b-s}(z)I_{b-n}(z)\}} = 0 \quad (6B)$$

$$\begin{aligned} \sigma_{2sn}(z) &= \sqrt{\overline{\text{LPF}^2\{2I_{b-s}(z)I_{b-n}(z)\}} - \mu_{2sn}^2(z)} \\ &= \sqrt{P_{Lo}P_S(z)}\sigma_{b-n} \quad (7B) \end{aligned}$$

3) The term of $\text{LPF}\{I_{b-n}^2(z)\}$ in (4).

Substituting (4B) into $\text{LPF}\{I_{b-n}^2(z)\}$, it can be obtained that:

$$\text{LPF}\{I_{b-n}^2(z)\} = \frac{1}{2}I_{b-n}^{I^2}(z) + \frac{1}{2}I_{b-n}^{Q^2}(z) \quad (8B)$$

As previously mentioned, both $I_{b-n}^I(z)$ and $I_{b-n}^Q(z)$ follow the zero-mean normal distributions with the same variance as that of $I_{b-n}(z)$ (shown by (3)). According to the calculation of n moments of a normal distribution [31], it can be obtained that:

$$\overline{I_{b-n}^{I^2}(z)} = \overline{I_{b-n}^{Q^2}(z)} = \sigma_{b-n}^2 \quad (9B)$$

and

$$\overline{I_{b-n}^{I^4}(z)} = \overline{I_{b-n}^{Q^4}(z)} = 3\sigma_{b-n}^4 \quad (10B)$$

The expectation value and STD of $\text{LPF}\{I_{b-n}^2(z)\}$, designated as $\mu_{n^2}(z)$ and $\sigma_{n^2}(z)$, respectively, can be calculated as:

$$\mu_{n^2}(z) = \overline{\text{LPF}\{I_{b-n}^2(z)\}} = \sigma_{b-n}^2 \quad (11B)$$

$$\begin{aligned} \sigma_{n^2}(z) &= \sqrt{\text{D}\left\{\frac{1}{2}I_{b-n}^{I^2}(z)\right\} + \text{D}\left\{\frac{1}{2}I_{b-n}^{Q^2}(z)\right\}} = \sigma_{b-n}^2 \\ & \quad (12B) \end{aligned}$$

where $\text{D}\{*\}$ represents the operator for evaluating the variance.

APPENDIX C

In this appendix, we present the detailed mathematical derivation from (11) to (12) and (13) in the main text, respectively, associated with their condition terms.

For *Region 1* in Section II as defined in the main text, where the polarization noise should dominate, it is required that:

$$\sigma_{s^2}^2(z) \gg \sigma_{2sn}^2(z) + \sigma_{n^2}^2(z) \quad (1C)$$

Substituting (6), (8) and (10) into (1C) gives rise to:

$$\begin{aligned} \frac{P_{Lo}^2 P_S^2(z)}{4} &\gg 2qP_{Lo}^2 P_S(z)B_F \\ & \quad + P_{Lo}P_S(z)\sigma_T^2 B_F \\ & \quad + 4q^2 P_{Lo}^2 B_F^2 \\ & \quad + \sigma_T^4 B_F^2 \\ & \quad + 4q\sigma_T^2 B_F^2 P_{Lo} \quad (2C) \end{aligned}$$

Keeping the dominating terms and removing the negligible terms in (2C), one can simplify (2C) to:

$$\frac{P_{Lo}^2 P_S^2(z)}{4} \gg 2qP_{Lo}^2 P_S(z)B_F + P_{Lo}P_S(z)\sigma_T^2 B_F \quad (3C)$$

Rearranging (3C) results in:

$$P_{Lo} [P_S(z) - 8qB_F] \gg 4\sigma_T^2 B_F \quad (4C)$$

which is taken as the condition term of (12) in the main text. When such a term is satisfied, (11) in the main text can be simplified to:

$$\text{SNR}(z) \approx \frac{\mu_{s^2}(z)\sqrt{M}}{\sigma_{s^2}(z)} = \sqrt{M} \quad (5C)$$

which corresponds to (12) in the main text.

On the other hand, for *Region 2* in Section II as defined in the main text, it can be mathematically derived that the squared detection noise $\sigma_{n^2}^2(z)$ dominates by considering parameters shown by the caption of Fig. 2 at the fiber far-end. In this case, (11) can be rewritten as:

$$\begin{aligned} \text{SNR}(z) &\approx \frac{\mu_{s^2}(z)\sqrt{M}}{\sigma_{n^2}(z)} \\ &\approx \frac{\frac{P_{Lo}P_S(z)}{2}\sqrt{M}}{\sigma_T^2 B_F + 2qP_{Lo}B_F} \\ &\approx \frac{\sqrt{M}}{\frac{2\sigma_T^2 B_F}{P_{Lo}P_S(z)} + \frac{4qB_F}{P_S(z)}} \quad (6C) \end{aligned}$$

It can be observed that P_{Lo} should be sufficiently large to maximize the SNR, to satisfy:

$$\frac{4qB_F}{P_S(z)} \gg \frac{2\sigma_T^2 B_F}{P_{Lo}P_S(z)} \quad (7C)$$

Keeping the dominating terms and removing the negligible terms in (2C), it can be simplified and rearranged to:

$$P_{Lo} \gg \frac{\sigma_T^2}{2q} \quad (8C)$$

which is taken as the condition term of (13) in the main text. When such a term is satisfied, (6C) can be further simplified to:

$$SNR(z) \approx \frac{\sqrt{M}}{\frac{4qB_F}{P_S(z)}} = \frac{\sqrt{M}P_S(z)}{4qB_F} \quad (9C)$$

APPENDIX D

In this appendix, we present the mathematical calculation of the theoretical minimum value of pulse peak powers required under a fixed OLO power of ~ 4 dBm in Section III-B. According to the statement of *Region 1* in Section II, it is necessary to satisfy (4C) at the fiber position of $z \approx 0$ (the impact of fiber loss is negligible for a short-distance sensing scenario) in order to reach the so-called polarization-noise-limit condition. Here we assume that $P_{Lo}[P_S(z=0) - 8qB_F] = 10 \cdot 4\sigma_T^2 B_F$ can be regarded as the critical condition at which $P_{Lo}[P_S(z=0) - 8qB_F]$ is much larger than $4\sigma_T^2 B_F$, namely:

$$P_{Lo}[P_S(z=0) - 8qB_F] = 40\sigma_T^2 B_F \quad (1D)$$

Substituting (1) into (1D), the required theoretical minimum pulse peak powers can be expressed as:

$$P_p^{min} = \frac{8N}{k_S c D_p^2} \left(\frac{5\sigma_T^2}{P_{Lo}} + q \right) \quad (2D)$$

For the distinct spatial resolutions of 1 m, 2 m and 6 m (corresponding to pulse durations of 10 ns, 20 ns and 60 ns, respectively), the calculation results of the required minimum pulse peak powers can be obtained as ~ 28.5 dBm, ~ 22.5 dBm, ~ 13.0 dBm, respectively, by substituting the value of each parameter into (2D).

REFERENCES

- [1] T. Kurashima, T. Horiguchi, H. Izumita, S. Furukawa, and Y. Koyamada, "Brillouin optical-fiber time domain reflectometry," *IEICE Trans. Commun.*, vol. 76, no. 4, pp. 382–390, 1993.
- [2] A. H. Hartog, *An Introduction to Distributed Optical Fibre Sensors*. Boca Raton, FL, USA: CRC, 2017.
- [3] M. A. Soto, "Distributed Brillouin sensing: Time-domain techniques," in *Handbook of Optical Fibers*. Cambridge, MA, USA: Academic Press, 2018, pp. 1–91.
- [4] Q. Bai et al., "Recent advances in Brillouin optical time domain reflectometry," *Sensors*, vol. 19, no. 8, 2019, Art. no. 1862.
- [5] A. Motil, A. Bergman, and M. Tur, "State of the art of Brillouin fiber-optic distributed sensing," *Opt. Laser Technol.*, vol. 78, pp. 81–103, 2016.
- [6] F. Wang, C. Zhu, C. Cao, and X. Zhang, "Enhancing the performance of BOTDR based on the combination of FFT technique and complementary coding," *Opt. Exp.*, vol. 25, no. 4, pp. 3504–3513, 2017.
- [7] J. Geng, S. Staines, M. Blake, and S. Jiang, "Distributed fiber temperature and strain sensor using coherent radio-frequency detection of spontaneous Brillouin scattering," *Appl. Opt.*, vol. 46, no. 23, pp. 5928–5932, 2007.
- [8] Y. Lu, R. Dou, and X. Zhang, "Wideband detection of spontaneous Brillouin scattering spectrum in Brillouin optical time-domain reflectometry," in *Proc. Int. Conf. Opt. Instruments Technol., Microelectron. Optoelectron. Devices Integration*, 2009, pp. 360–366.
- [9] K. Shimizu, T. Horiguchi, Y. Koyamada, and T. Kurashima, "Coherent self-heterodyne Brillouin OTDR for measurement of Brillouin frequency shift distribution in optical fibers," *J. Lightw. Technol.*, vol. 12, no. 5, pp. 730–736, May 1994.
- [10] X. Feng, J. Zhou, C. Sun, X. Zhang, and F. Ansari, "Theoretical and experimental investigations into crack detection with BOTDR-distributed fiber optic sensors," *J. Eng. Mechanics*, vol. 139, no. 12, pp. 1797–1807, 2013.
- [11] K. Shimizu, T. Horiguchi, Y. Koyamada, and T. Kurashima, "Coherent self-heterodyne detection of spontaneously Brillouin-scattered light waves in a single-mode fiber," *Opt. Lett.*, vol. 18, no. 3, pp. 185–187, 1993.
- [12] Q. Wang, Q. Bai, Y. Liu, J. Wang, Y. Wang, and B. Jin, "SNR enhancement for BOTDR with spatial-adaptive image denoising method," *J. Lightw. Technol.*, vol. 41, no. 8, pp. 2562–2571, Apr. 2023.
- [13] T. Horiguchi and M. Tateda, "BOTDA-nondestructive measurement of single-mode optical fiber attenuation characteristics using Brillouin interaction: Theory," *J. Lightw. Technol.*, vol. 7, no. 8, pp. 1170–1176, Aug. 1989.
- [14] T. Kurashima, T. Horiguchi, and M. Tateda, "Distributed-temperature sensing using stimulated Brillouin scattering in optical silica fibers," *Opt. Lett.*, vol. 15, no. 18, pp. 1038–1040, Sep. 1990.
- [15] A. Zadok, X. Bao, Z. Yang, and L. Thévenaz, "SBS-based fiber sensors," in *Brillouin Scattering Part 2*, (Series Semiconductors and Semimetals), vol. 110, B. J. Eggleton, M. J. Steel, and C. G. Poulton, Eds., Amsterdam, The Netherlands: Elsevier, 2022, pp. 1–52.
- [16] M. A. Soto and L. Thévenaz, "Modeling and evaluating the performance of Brillouin distributed optical fiber sensors," *Opt. Exp.*, vol. 21, no. 25, pp. 31347–31366, 2013.
- [17] S. Wang, Z. Yang, M. A. Soto, and L. Thévenaz, "Study on the signal-to-noise ratio of Brillouin optical-time domain analyzers," *Opt. Exp.*, vol. 28, no. 14, pp. 19864–19876, 2020.
- [18] X. Gao et al., "Impact of optical noises on unipolar-coded Brillouin optical time-domain analyzers," *Opt. Exp.*, vol. 29, no. 14, pp. 22146–22158, 2021.
- [19] X. Sun et al., "Genetic-optimised aperiodic code for distributed optical fibre sensors," *Nature Commun.*, vol. 11, no. 1, 2020, Art. no. 5774.
- [20] N. Lalam, W. P. Ng, X. Dai, Q. Wu, and Y. Q. Fu, "Performance improvement of Brillouin ring laser based BOTDR system employing a wavelength diversity technique," *J. Lightw. Technol.*, vol. 36, no. 4, pp. 1084–1090, Feb. 2018.
- [21] C. Li, Y. Lu, X. Zhang, and F. Wang, "SNR enhancement in Brillouin optical time domain reflectometer using multi-wavelength coherent detection," *Electron. Lett.*, vol. 48, no. 18, pp. 1139–1141, 2012.
- [22] N. Lalam, W. P. Ng, X. Dai, Q. Wu, and Y. Q. Fu, "Performance analysis of Brillouin optical time domain reflectometry (BOTDR) employing wavelength diversity and passive depolarizer techniques," *Meas. Sci. Technol.*, vol. 29, no. 2, 2018, Art. no. 025101.
- [23] Y. Lu, Y. Yao, X. Zhao, F. Wang, and X. Zhang, "Influence of non-perfect extinction ratio of electro-optic modulator on signal-to-noise ratio of BOTDR," *Opt. Commun.*, vol. 297, pp. 48–54, 2013.
- [24] Q. Bai et al., "Enhancing the SNR of BOTDR by gain-switched modulation," *IEEE Photon. Technol. Lett.*, vol. 31, no. 4, pp. 283–286, Feb. 2019.
- [25] R. W. Boyd, A. L. Gaeta, and E. Giese, "Nonlinear optics," in *Springer Handbook of Atomic, Molecular, and Optical Physics*. Berlin, Germany: Springer, 2008, pp. 1097–1110.
- [26] B. E. Saleh and M. C. Teich, *Fundamentals of Photonics*. Hoboken, NJ, USA: Wiley, 2019.
- [27] M. Alem, M. A. Soto, and L. Thévenaz, "Analytical model and experimental verification of the critical power for modulation instability in optical fibers," *Opt. Exp.*, vol. 23, no. 23, pp. 29514–29532, 2015.
- [28] S. Zaslowski, Z. Yang, and L. Thévenaz, "On the 2D post-processing of Brillouin optical time-domain analysis," *J. Lightw. Technol.*, vol. 38, no. 14, pp. 3723–3736, Jul. 2020.
- [29] R. Hui and M. O'Sullivan, *Fiber-Optic Measurement Techniques*. Cambridge, MA, USA: Academic Press, 2022.
- [30] A. Yariv and P. Yeh, *Photonics: Optical Electronics in Modern Communications*. London, U.K.: Oxford Univ. Press, 2007.
- [31] R. A. Johnson, I. Miller, and J. E. Freund, *Probability and Statistics for Engineers*, vol. 2000. London, U.K.: Pearson Educ., 2000.